# Implementation and Motion Control of a Microrobot Using Laser Sensors

Konstantinos Karaiskos, Charalampos Lampousis, Kostas Vlachos, *Member, IEEE*, and
Evangelos Papadopoulos, *Fellow, IEEE*

*Abstract*— In this paper an improved implementation of a microrobotic platform, including position feedback provided by two laser sensors, and the development of a rule-based closed-loop motion controller are presented. The microrobot employs a novel driving principle, using centrifugal forces generated by two vibration motors that give the platform the ability to make motions with micrometer resolution. In this implementation, a pair of laser sensors are integrated at the bottom of the platform and calibrated through a custom procedure. The high-rate output of the laser sensors is fed to an algorithm that provides the position and orientation of the microrobot required for closed-loop motion control. Compared to using an overhead camera, this implementation, results in up to five times higher closed-loop control bandwidth, improved autonomy, and modularity. Experimental closed-loop results demonstrate the ability of the motion controller in driving the microrobot to a desired target under a microscope.

## I. INTRODUCTION

Micro robotics is an interdisciplinary field that combines many aspects of robotics, with an emphasis in small scale. Due to the great advances in conventional robotics and microsystem technology (MST) there is a growing need for miniaturized robots (of size in the order of square centimeters) and microrobots worldwide. The development of remote-controlled or even autonomous microrobots will lead to pervasive advances in many areas, such as in medicine (microsurgery), manufacturing (microassembly, inspection and maintenance), and biology (cell handling).

Micro-manipulation by microrobots has gained a lot of attention in industry and biomedicine, for tasks exceeding human capacity. The handling of biological cells [1], or the assembly of a microsystem consisting of various microstructures are good examples [2]. A popular micro-positioning motion mechanism is the stick-slip principle, which is implemented using piezoelectric actuators. This principle was employed by the MINIMAN microrobot [3] and MiCRoN which employs piezoelectric actuators with an integrated micro-manipulator [4]. A different motion mechanism based on piezo tubes was utilized by the Nano Walker microrobot [5]. A micro-bristle-bot fabricated by two-photon lithography using PZT actuators has been presented [6]. Piezoelectric actuators give the ability to

microbots to perform motion of high resolution, in the scale of nanometers; however, they suffer from complex and high-cost power units.

The design of a novel microrobotic platform was proposed, circumventing the limitations of piezoelectric actuators [7]. The motion principle is based on two vibration motors, giving the ability to the platform to perform non-holonomic translation and rotation, with micrometer resolution. A similar actuation principle was used in the Rizeh [8] and the Kilobot, designed to study collective behaviors [9]. Robotic Swarms, implementing different actuation and motion principles were introduced in [10] and [11]. The use of a reinforcement learning framework for the autonomous navigation of a group of microrobots in a multi-agent collaborative environment has been proposed in [12]. The use of a single vibration motor on a microrobot that can perform two-dimensional motion has been studied in [13].

Regarding the localization system, the development of an odometry system for wheeled robots using optical sensors was proposed in [14]. The authors suggested a calibration procedure, and a sensor fault correction system. Optimization techniques for the placement of the sensors, and a calibration procedure using least squares algorithm have been proposed in [15] and [16].

This paper focuses on the integration of a pair of laser sensors in an improved hardware design of the microrobot introduced in [17], and on its motion control, based on the feedback acquired from it. Compared to the use of an overhead camera with a loop time of more than 100 ms, this implementation, results in up to five times higher closed-loop control bandwidth, lower cost, improved autonomy, and modularity. The capability for on-board calculations extends the modularity and usefulness of the microrobotic platform. Experimental closed-loop results demonstrate the ability of the motion controller in driving the microrobot to a desired target under a microscope.

## II. SYSTEM OVERVIEW

A brief description of the microrobot is given here. The innovative actuation principle of the microrobot is elaborated in [7] and for a more detailed presentation of the dynamics of the microrobot, see [19].

To illustrate the motion principle of the microrobot, a simplified 1 DOF mobile platform of mass M is used, whose motion mechanism is made of an eccentric mass m, rotated by a platform-mounted motor O, see Fig. 1. The mass $m$ rotates on a vertical plane at a constant speed $\omega$, and the platform is constrained to move along the Y-axis only.

K. Karaiskos, C. Lampousis, and E. Papadopoulos are with the School of Mechanical Engineering, National Technical University of Athens, Athens, 15780 Greece (e-mail: egpapado@central.ntua.gr).

K. Vlachos is with the Department of Computer Science & Engineering, University of Ioannina, Ioannina, 45110 Greece, (e-mail: kostaswl@cse.uoi.gr).

One cycle of operation is completed when the mass $m$ has described an angle of 360°. Gravitational and centripetal forces exerted on the rotating mass are resolved along the Y-Z axes to yield

$$f_{oy} = m\omega_m^2 r \sin\theta \qquad (1)$$

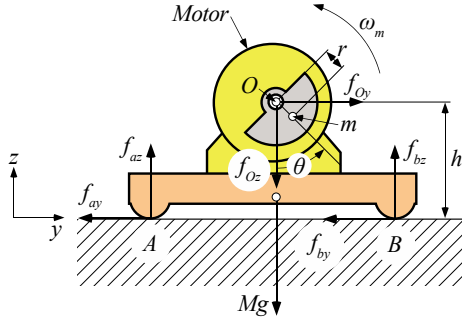$$f_{oz} = -mg - m\omega_m^2 r \cos\theta \qquad (2)$$



Fig. 1. Simplified 1 DOF platform with rotating mass.

where $\theta$ is the rotation angle of the eccentric mass, g is the acceleration of gravity, and r is the length of the link between m and O (see Fig. 1). If the rotational speed exceeds a critical value, $f_{Oy}$ overcomes static friction forces and the platform begins to slide. For a counterclockwise rotation of the eccentric mass m, the platform exhibits a net displacement toward the positive Y-axis. It has been shown analytically that the motion step that the platform exhibits over a cycle of operation can be made arbitrarily small depending on the actuation speed $\omega$, [7]. In practice, the motion resolution is limited by the electronic driving modules and by the unknown nonuniform distribution of the coefficient of friction $\mu$ along the surface of motion.

The actuation principle mentioned earlier was employed in the design and implementation of a 2-DOF microrobot, with two vibration motors, as shown in Fig. 2.
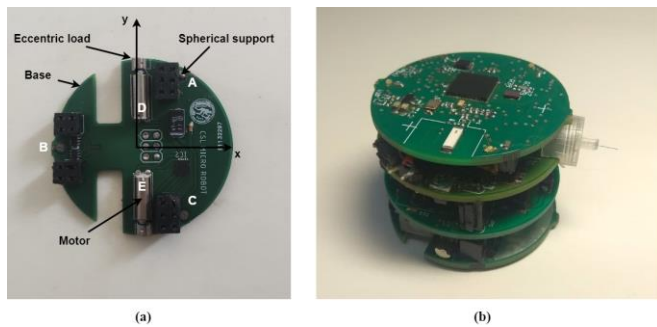


Fig. 2. (a) Base design; (b) prototype.

If both actuators have the same speed, then the platform can move along the body-fixed x-axis or rotate about its center of mass (CM) depending on the sense of rotation of the actuators.

Using the Newton–Euler formulation, the platform dynamics are described by:

$$M\dot{\mathbf{v}} = \mathbf{R}_b \sum_i {}^b\mathbf{f}_i, \quad i = A, B, C, D, E \qquad (3)$$

$$I\dot{\omega}_p = \sum_i ({}^b\mathbf{r}_i \times {}^b\mathbf{f}_i)\cdot\hat{\mathbf{z}} \quad i = A, B, C, D, E \qquad (4)$$

where i = {A, B, C, D, E}, see Fig. 2. The ${}^b\mathbf{f}_i$ are the forces (friction and motor forces) acting on the platform, $\mathbf{R}_b$ is a rotation matrix from the body-fixed frame to the inertial frame, $\omega_p$ is the platform angular velocity, $I$ is its moment of inertia, $\mathbf{v}$ is its CM inertial velocity, ${}^b\mathbf{r}_i$ are vectors from the CM to the ${}^b\mathbf{f}_i$, and $\hat{\mathbf{z}}$ the unit vector normal to the plane of motion. The left superscript $b$ denotes a body-fixed frame; a missing left superscript denotes the inertial frame.

## III. MECHATRONIC SYSTEM IMPLEMENTATION

The micro robotic platform, with a diameter of 4.3 cm and a height of 3.3 cm, consists of four printed circuits boards (PCBs) as shown in Fig. 3.
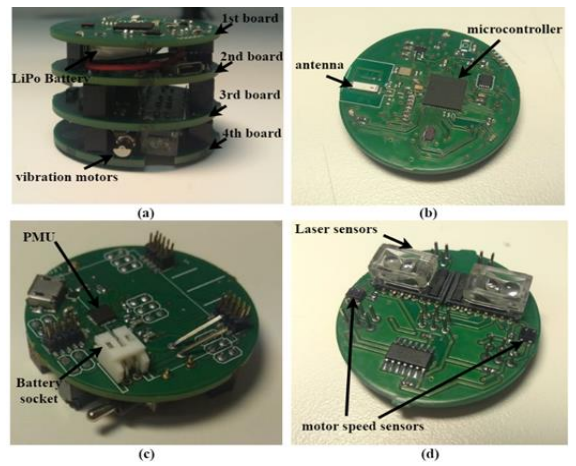


Fig. 3. The microrobotic platform and three of its four PCBs.

The first board constitutes the core of the robot as it contains the microcontroller responsible for all its functions, see Fig. 3(b). Also, it includes an RF antenna and its electronics to communicate wirelessly with an external computer. The second board includes a 3.7V Li-Po battery, a power management unit (PMU) TPS65721 and all necessary components to power the controller, the motors, the sensors, and other electronic components of the robot, see Fig. 3(c). The third board is the sensor board which contains the position sensor ADNS-7550 and the motor speed sensor QRE1113, see Fig. 3(d). The ADNS-7550 sensor is an integrated mouse sensor with a low power consumption (~20 mA), high speed motion detection up to 30 ips, a weight of 8g, and 5 different cpi resolutions. The fourth board is responsible for its movement as it includes two vibration micromotors, axially coupled to an eccentric load, the driving unit A3901, and three contact points between the platform and the ground, provided by three small, fixed steel balls, see Fig. 2(a). The robot is equipped with a needle, the tip of which is its end point.

## IV. LOCALIZATION USING LASER SENSORS

### A. Odometry analysis

In this section, the use of two laser sensors for the localization (position and orientation) of the platform is described. Fig. 4 shows the microrobotic platform

displacement and orientation in two consecutive time samples. In this figure, the following are defined and shown:

- $\{O_w\}$ is the inertial coordinate system (CS),
- $\{O_r\}$ is the coordinate system of the robot located at the point of interest R. In this case, it is attached at the middle point of the line connecting the two sensors.
- $\{O_{s,l}\}$ and $\{O_{s,r}\}$ are the coordinate systems attached at the left and right laser sensors, respectively.
- $\Delta O_{s,l}$ and $\Delta O_{s,r}$ denote the displacements vectors of the left and right sensors respectively, in $\{O_w\}$.
- $\Delta O_R$ is the displacement of the robot in $\{O_w\}$,
- $\xi$ is the angle between the x-axis of $\{O_r\}$ and the normal to the line connecting the two sensors
- $\varphi_{r/l}$ is the orientation of each sensor with respect to the x-axis of $\{O_r\}$, and
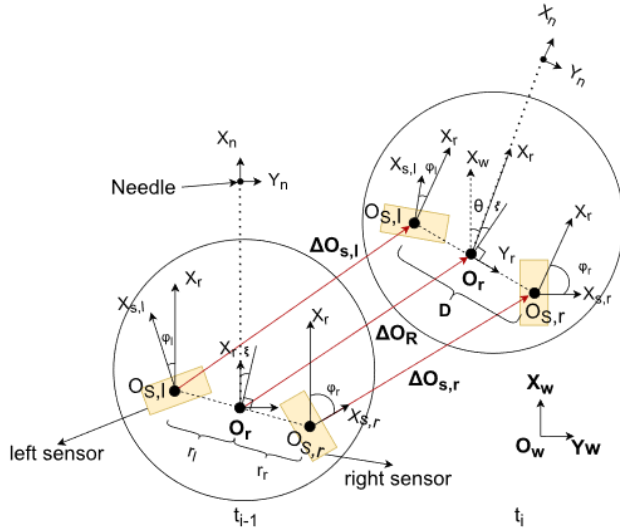- $\theta$ is the orientation of the robot with respect to $\{O_w\}$.



Fig. 4. The microrobotic platform at two consecutive time instances.

The displacement of each sensor, $\Delta O_s$ with respect to $\{O_w\}$, at sampling time (i), is given by

$$\Delta O_{S,r/l(i)} = \mathbf{R}_S(\theta_{i-1} + \varphi_{r/l}) \cdot \Delta O_{S,r/l(i)}^S \tag{5}$$

where $\mathbf{R}_S$ is the rotation matrix of $\{O_s\}$ with respect to $\{O_w\}$, and r/l indicates right or left. (5) can be expressed as:

$$\Delta O_{S,r/l(i)} = \begin{pmatrix} \cos(\theta_{i-1} + \varphi_{r/l}) & -\sin(\theta_{i-1} + \varphi_{r/l}) \\ \sin(\theta_{i-1} + \varphi_{r/l}) & \cos(\theta_{i-1} + \varphi_{r/l}) \end{pmatrix} \begin{pmatrix} \Delta X_{S,r/l(i)}^S \\ \Delta Y_{S,r/l(i)}^S \end{pmatrix} \tag{6}$$

where $\Delta X^s_s$, $\Delta Y^s_s$ are the sensor's relative displacements, in x and y axis, with respect to $\{O_S\}$ in two consecutives time samples $t_{i-1}$, $t_i$ (Fig. 4). Finally, the position vector $[X_s, Y_s]$ of each sensor is given by:

$$\begin{pmatrix} X_{S,r/l(i)} \\ Y_{S,r/l(i)} \end{pmatrix} = \Delta O_{S,r/l(i)} + \begin{pmatrix} X_{S,r/l(i-1)} \\ Y_{S,r/l(i-1)} \end{pmatrix} \tag{7}$$

Since the sensors are placed at a fixed point on the robot platform, the position vector $[X_R, Y_R]$ respect to $\{O_w\}$ is

$$\begin{pmatrix} X_R \\ Y_R \end{pmatrix} = \begin{pmatrix} X_{S,r/l} \\ Y_{S,r/l} \end{pmatrix} - \mathbf{R}_R(\theta)O_{S,r/l}^R \tag{8}$$

where $\mathbf{R}_R$ is the rotation matrix of $\{O_r\}$ with respect to $\{O_w\}$ and $O^R_S$ is a vector that represents the constant

transformation from the $\{O_r\}$ to $\{O_s\}$ and is expressed by the relation

$$O_{S,r}^R = [-r_r \sin(\xi), r_r \cos(\xi)]^T$$
$$O_{S,l}^R = [r_l \sin(\xi), -r_l \cos(\xi)]^T \tag{9}$$

where $r$ is the distance between a sensor and the $\{O_r\}$. Since the origin of $\{O_r\}$ is chosen at the middle of the line connecting the two sensors, using (8) for the left sensor, the robot's position coordinates $X_R$ and $Y_R$, can be expressed as

$$X_R = X_{S,l} - r_l \sin(\theta + \xi) \tag{10}$$

$$Y_R = Y_{S,l} + r_l \cos(\theta + \xi) \tag{11}$$

and using the right sensor

$$X_R = X_{S,r} + r_r \sin(\theta + \xi) \tag{12}$$

$$Y_R = Y_{S,r} - r_r \cos(\theta + \xi) \tag{13}$$

Combining (10) - (13) and taking into consideration that $r_r = r_l$ the following holds

$$X_R = \frac{X_{S,l} + X_{S,r}}{2} \tag{14}$$

$$Y_R = \frac{Y_{S,l} + Y_{S,r}}{2} \tag{15}$$

Therefore, the position of point R is given by the average of sensor values. Finally, the position estimation of the end point of the robot (see Fig. 4), i.e., the tip of the needle coordinates $X_n$, $Y_n$, are calculated as:

$$\begin{pmatrix} X_n \\ Y_n \end{pmatrix} = \begin{pmatrix} X_R \\ Y_R \end{pmatrix} + \mathbf{R}_R(\theta) \begin{pmatrix} \rho \\ 0 \end{pmatrix} \tag{16}$$

where $\rho$ is the distance between the origin of $\{O_r\}$ and the tip of the needle, see Fig. 4.

According to Fig. 5 the orientation can be expressed as:

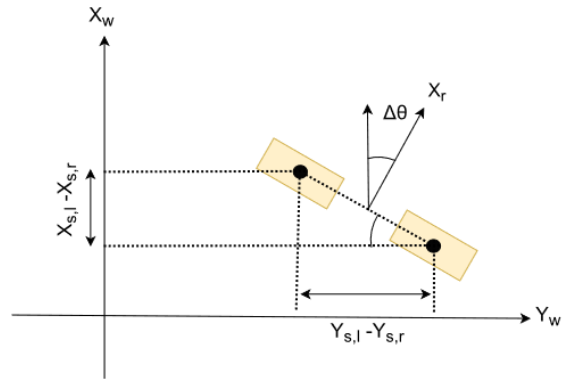$$\theta = a \tan 2(X_{S,l} - X_{S,r}, Y_{S,r} - Y_{S,l}) \tag{17}$$



Fig. 5. Orientation between two consecutive time steps.

B. *Calibration process*

To reduce systematic errors, a calibration process is employed, with the microrobot constrained to move either along a straight line, or around a fixed axis, see Fig. 6. The values estimated through this process include the counts acquired by the sensor for a known displacement, i.e., counts per inch (cpi), the distance D between the two sensors, and the orientation of each sensor $\varphi_{r/l}$. Angle $\xi$ was assumed by design to be zero.
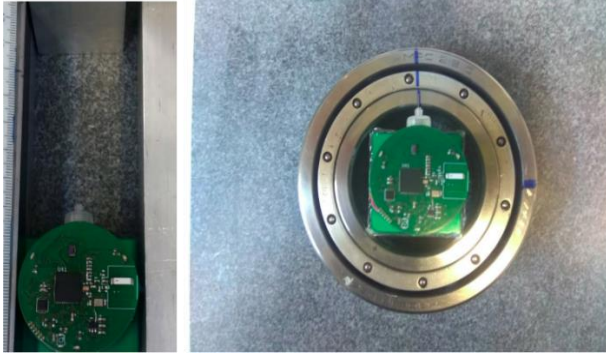
Fig. 6. Calibration experiment setup. (a) the straight-line, (b) rotation.

### 1) Straight line displacement experiment

To determine the cpi and the angle $\varphi$ of each sensor, an experiment was performed (Fig. 6(a)), which consisted of linearly translating the platform's body for a known length along the $X_R$-axis. As the platform moves along the x-axis, the two sensors acquire the equivalent displacements with respect to $\{O_s\}$, $(\Delta X^s{}_{S_r}, \Delta Y^s{}_{S_r})$ and $(\Delta X^s{}_{S_l}, \Delta Y^s{}_{S_l})$ (Fig. 7). With this procedure the factor k (one for each sensor) is estimated that must be multiplied by the sensor number of counts, to convert them into inch units.
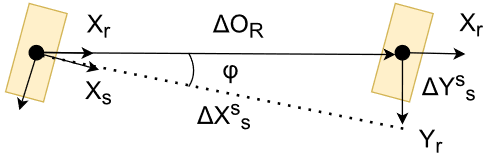


Fig. 7. Straight-line calibration experiment. The robot translates in a straight line for $\Delta O_R$ mm, and each sensor acquires measurements $\Delta X^s{}_s$ and $\Delta Y^s{}_s$.

$$k_{r/l} = \frac{\Delta O_R}{\sqrt{(\Delta X^S_{S,r/l})^2 + (\Delta Y^S_{S,r/l})^2}} \qquad (18)$$

Using the same measurements, the angle $\varphi$ can be calculated for each sensor:

$$\varphi_{r/l} = a\tan 2(\Delta Y^S_{S,r/l}, \Delta X^S_{S,r/l}) \qquad (19)$$

### 2) Rotation experiment

To determine the distance D between the laser sensors, a rotation experiment of the platform about a fixed axis and for a known angle $\theta$, is being performed, by means of constraining the microrobot in a cylindrical part, see Fig. 6(b).

Fig. 8 shows a rotation of the robot around the center of rotation (CR) for a known angle $\theta$. $\Delta X^s{}_s$ and $\Delta Y^s{}_s$ are the displacements of the sensors with respect to the sensors body frame in x and y axis. Then, the total length of the distances, $L_l$ and $L_r$, travelled by each sensor can be approximated as (see Fig 8(a)):

$$L_{r/l} = \sqrt{(\Delta X^S_{S,r/l})^2 + (\Delta Y^S_{S,r/l})^2} \qquad (20)$$

As the sampling time is sufficient small, we can assume that the distance $L$ (of each sensor) is the arc that forms the sensors at its rotation. Knowing the length of the arc and the rotation angle $\theta$, the sensors' distance from the fixed center of rotation, a, is calculated by:

$$a_{r/l} = \frac{L_{r/l}}{\theta} \qquad (21)$$
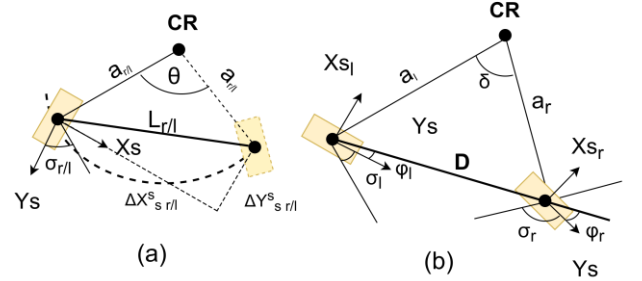


(a)            (b)

Fig. 8. Rotational calibration experiment.

As the center of rotation is not the middle of the line connecting the two sensors, $D \neq a_l + a_r$. Therefore, to find the distance, the angle $\sigma$ between the tangent of the arc that is formed by the motion and the Y-axis of each sensor (see Fig. 8(a)), is given by:

$$\sigma_{r/l} = a\tan 2(\Delta X^S_{S,r/l}, \Delta Y^S_{S,r/l}) \qquad (22)$$

Finally, the distance D (see Fig. 8(b)) is calculated as:

$$D = \sqrt{a_r^2 + a_l^2 - 2a_r a_l \cos(\delta)} \qquad (23)$$

where

$$\delta = |(\sigma_r + \varphi_r) - (\sigma_l + \varphi_l)| \qquad (24)$$

Performing the above routine, the unknown parameters are estimated as: $k_r = 1840$ cpi, $k_l = 1804$ cpi, $\varphi_r = -0.77°$, $\varphi_l = 1.04°$ and $D = 2.1$cm.

### C. Accuracy experiments

To determine the accuracy of the sensors and the localization algorithm, we perform experiments in straight line motion and in pure rotation. For the first validation test, the microrobot moves in a known straight line back and forth. Three different displacements were tested, i.e., 3 cm (Fig. 9(a)), 6.4 cm (Fig. 9(b)), and 10 cm (Fig. 9(c)). From the results is concluded that the deviation in X-axis is very small. The main error concerns the Y-axis, where a deviation of 0.8mm, 1.5mm and 2.1mm respectively is observed. As expected, the greater the displacement, the larger the deviation along the Y-axis, due to the accumulative nature of the sensor use and the small error in orientation $\theta$.

In the rotational experimental test, a 90° rotation was performed. The deviation during this test was less than 5°, see Fig 10. The calibration routine was tested by collecting data from the sensors and introducing them into the positioning algorithms. More specifically, a 90° rotation experiment was performed, during which two different values of the distance D were introduced into the algorithm; the first value corresponded to the distance found by the calibration process and the other with a deviation of 3 mm as given by measuring the distance. Fig. 11 shows that a 3 mm deviation of the distance D leads to an incorrect orientation estimation of 10°. Moreover, a straight-line trajectory was studied, validating the error correction due to the angle $\varphi$ calibration. As Fig. 11 indicates, the angle $\varphi$ has minor effect on the Y-axis error, because sensors are placed such that $\varphi \approx 0$.
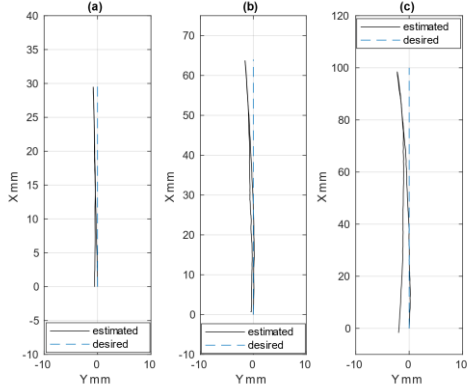
Fig. 9. Straight line accuracy experiments. Platform tested in three different distances (3cm, 6.4cm, 10cm).
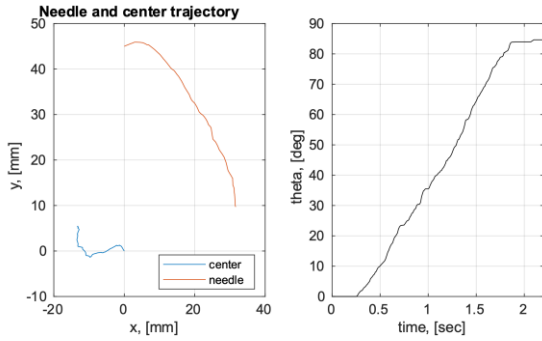

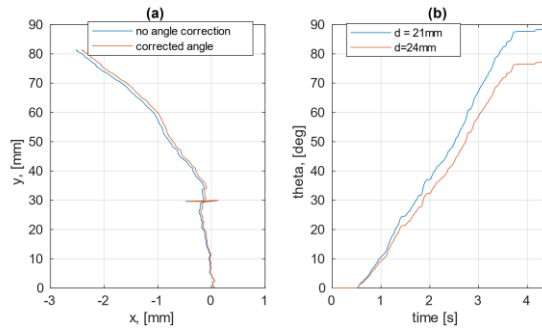
Fig. 10. 90° rotation accuracy experiment.



Fig. 11. Calibration correction experiments. (a) Correction of the straight-line motion estimation due to angle $\varphi$ estimation, (b) correction of the orientation estimation due to D calibration.

## V. MOTION CONTROL

For the motion control of the platform, a rule-based closed loop control algorithm, was used [17]. The basic idea is presented in (25) and consists of three distinct pairs of motor angular velocities, $(\omega_{d*}, \omega_{e*})$, $(\omega_{d\downarrow}, \omega_{e\downarrow})$ and $(\omega_{d\uparrow}, \omega_{e\uparrow})$. The goal is to keep the microrobot inside a tolerance zone, of width $2\varepsilon$, as it follows a desired path, i.e., a straight line.

$$\begin{pmatrix} \omega_d \\ \omega_e \end{pmatrix} = \begin{matrix} (\omega_{d\downarrow}, \omega_{e\downarrow})^T & y < y_{des} - \varepsilon \\ (\omega_{d*}, \omega_{e*})^T & \text{if } y_{des} - \varepsilon < y < y_{des} + \varepsilon \\ (\omega_{d\uparrow}, \omega_{e\uparrow})^T & y > y_{des} + \varepsilon \end{matrix} \qquad (25)$$

The first pair, $(\omega_{d*}, \omega_{e*})$, is applied to the motors of the microrobot when it is within the tolerance zone and corresponds to a straight-line motion. However, various sources of disturbances (microrobot asymmetries, errors in actuation synchronization, nonuniform distribution of friction) lead to parasitic motion that drives the robot outside the tolerance zone. To drive the robot inside the zone again, the other two pairs of motor angular velocities, $(\omega_{d\downarrow}, \omega_{e\downarrow})$ and $(\omega_{d\uparrow}, \omega_{e\uparrow})$, are applied, depending on the needed positive or negative instantaneous curvature. Eventually, the microrobot is stopped when a desired target point inside the tolerance zone is reached.

To determine the appropriate angular velocity pairs of $\omega_d$ and $\omega_e$, which depend on system parameters, for the implementation of the algorithm, open loop experiments were performed, see Fig. 12. The pairs were estimated in PWM to be $(\omega_{d*}, \omega_{e*}) = (26\%, 28\%)$, $(\omega_{d\downarrow}, \omega_{e\downarrow}) = (28\%, 20\%)$ and $(\omega_{d\uparrow}, \omega_{e\uparrow}) = (20\%, 27\%)$. Tolerance zone is selected to be 0.2mm., simulating the tip of a needle.
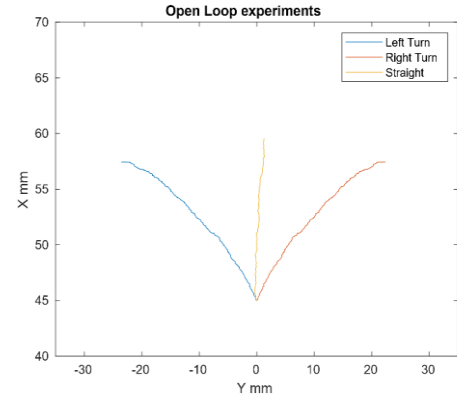


Fig. 12. Open loop experiments to determine angular velocities $\omega_d$ and $\omega_e$, for the purpose of the motion control.

In our setup, the goal of the microrobot is to move under a microscope using the laser sensors for position and orientation feedback, see Fig. 13. This decreases the loop time by a factor of five, compared to that with an overhead camera. The control algorithm has been experimentally evaluated using the two laser sensors for feedback. The experimentation scenario was to place the microrobot 1.5 cm away from a certain target point and test its ability to reach a circular area centered on the target point with a radius of 1.5 mm. The size of this area corresponds to the microscope field of view, see Fig. 13.

To validate the localization capability of the laser sensors, and the motion controller, the motion of the microrobot's end point was recorded by an external camera. The end point of the robot is the tip of a needle attached on it, and it was placed 48 mm away from the center of the robot, along the x-axis. Therefore, the initial position of the end point, is (x, y) = (48, 0). During the experiment, the laser sensors feedback output was transmitted through RF communication and saved on a PC for post-processing.

At the same time, the position of the microrobot's end point in pixels is acquired by an external camera. By measuring the actual distance of the center of the robot from the tip of the needle, we find the transformation ratio $\lambda$ for converting pixels into mm, see Fig. 14

$$\lambda = \frac{D_{real}}{D_{pixel}} = \frac{39.5mm}{250\ pixel} = 0.158mm\ /\ pixel \qquad (26)$$
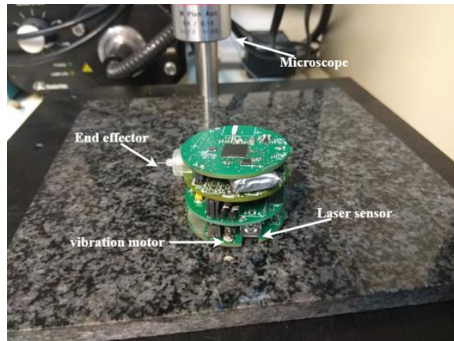
Fig. 13. The overall working configuration includes the computer, the workspace, the microscope with special camera and the robot itself.
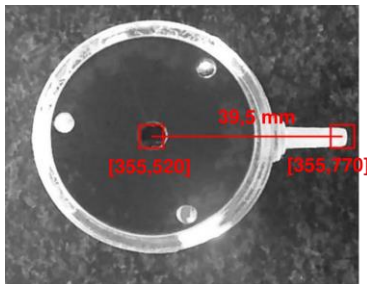


Fig. 14. Distance (in pixels) of the center of the robot from the tip of the needle. Camera computer vision algorithm provides the equivalent pixels.

Fig. 15 shows the microrobot position estimation by the laser sensors, as well as the recordings of the camera. The error of the laser sensors is about 1 mm, while the motion controller has a positioning error of about 0.3 mm, alongside the y-axis. Despite this error, the microrobot successfully enters the microscope field of view.
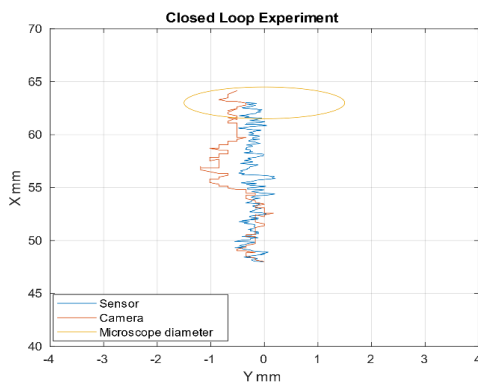


Fig. 15. Microrobot path as captured by the laser sensors and the camera.

## VI. CONCLUSION

This paper presented the development of a two-laser sensor localization system for the position control of a microrobotic platform, and the implementation of a rule-based closed-loop motion controller. The microrobot employs a novel driving principle, i.e., it uses centrifugal forces generated by two vibration motors endowing the platform with the ability to make motions with micrometer resolution. A pair of laser sensors were integrated at the bottom of the platform and calibrated through a custom procedure. The high-rate output of the laser sensors is fed to an algorithm that provides the position and orientation of the microrobot required for closed-loop motion control. It was demonstrated that the localization system achieves high accuracy and allows on-board implementation of the algorithm, avoiding the shortcoming of low bandwidth feedback provided by an external camera, increasing it up to five times. A closed-loop motion control algorithm was tested experimentally, driving successfully the microrobot to its goal.

## REFERENCES

[1] Tagliareni F. et al., "Manipulating biological cells with a micro-robot cluster," *IEEE/RSJ International Conference on Intelligent Robots and Systems (IROS '05)*, 2-6 Aug. 2005, pp. 1414 – 1419.

[2] Fatikow, S., & Benz, M. (1998). "A microrobot-based automated micromanipulation station for assembly of microsystems." *Computers in Industry*, 36(1-2), 155–162.

[3] Schmoeckel, F., and S. Fatikow, "Smart flexible microrobots for Scanning Electron Microscope (SEM) applications," *J. Intell. Mater. Syst. Structures,* vol. 11, no. 3, pp. 191–198, 2000.

[4] Brufau, J., and M. Puig-Vidal et al., "MICRON: Small autonomous robot for cell manipulation applications," *IEEE Int. Conference on Robotics and Automation*, Barcelona, Spain, Apr. 18–22, 2005, pp. 844–849.

[5] Martel, S., et al. "Three-legged wireless miniature robots for mass-scale operations at the sub-atomic scale," *IEEE International Conference on Robotics and Automation,* Seoul, 2001.

[6] Kim, D., Hao, Z., Ueda, J., & Ansari, A. "A 5mg micro-bristle-bot fabricated by two-photon lithography," *Journal of Micromechanics and Microengineering*, v. 29, n 10, Aug. 2019.

[7] Vartholomeos, P., and E. Papadopoulos, "Dynamics, design and simulation of a novel microrobotic platform employing vibration microactuators," *J. Dynamic Systems, Measurement, and Control*, ASME, vol. 128, pp.122–134, March 2006.

[8] Akbarimajd, A., & Sotoudeh, N. (2013), "Design and motion analysis of vibration-driven small robot Rizeh," *Advanced Robotics*, 28(2), 105–117.

[9] Rubenstein M., Radhika Nagpal. "KiloBot: A Robotic Module for Demonstrating Collective Behaviors," *Modular Robotics Workshop, IEEE International Conference on Robotics and Automation*, 2012.

[10] Kim, J.Y., T. Colaco, Z. Kashino, G. Nejat, and B. Benhabib, "mROBerTO: A modular millirobot for swarm-behavior studies," *IEEE/RSJ International Conference on Intelligent Robots and Systems (IROS '16),* 2016, pp. 2109-2114.

[11] Jang, H.B., R. D. Villalba, D. Paley, and S. Bergbreiter, "RSSI-based rendezvous on the tiny terrestrial robotic platform (TinyTeRP)," *Inst. Syst. Research and Tech. Rep.*, Univ. Maryland, Aug. 2013

[12] Chaysri, P., Blekas, K., & Vlachos, K., "Multiple mini-robots navigation using a collaborative multiagent reinforcement learning framework," *Advanced Robotics*, 34:13, 2020, 902-916.

[13] Ju, J., Wang, Q., & Zhang, K. (2018). Design and analysis of a novel micro-robot driving platform. *Proceedings of the Institution of Mechanical Engineers, Part C: Journal of Mechanical Engineering Science*, 095440621880231.

[14] Bonarini A., Matteucci M., and Restelli M., "A kinematic-independent dead-reckoning sensor for indoor mobile robotics," *IEEE/RSJ Int. Conference on Intelligent Robots and Systems*, vol. 4, pp. 3750–3755.

[15] Cimino Mauro and Pagilla R. Prabhakar, "Location of optical mouse sensors on mobile robots for odometry," *IEEE Int. Conf. Robotics and Automation*, May 3-8, 2010, Anchorage, Alaska, USA, pp 5429-5434.

[16] Paijens, A. F. M., Huang, L., & Al-Jumaily, A. M., "Implementation and calibration of an odometry system for mobile robots, based on optical computer mouse sensors," *Sensors and Actuators A: Physical*, 301, 111731, 2020.

[17] Vartholomeos P., Vlachos K., and Papadopoulos E., "Analysis and motion control of a centrifugal-force microrobotic platform," *IEEE Trans. Autom. Sci. Eng.*, 10(3), 2013, pp. 545–553.

[18] Sciavicco, L., and B. Siciliano, *Modelling and Control of Robot Manipulators*. New York: Springer-Verlag, 2001.

[19] Vartholomeos, P., and E. Papadopoulos, "Analysis, design and control of a planar micro-robot driven by two centripetal-force actuators," *IEEE International Conference on Robotics and Automation (ICRA'06)*, Orlando, FL, USA, May 15–19, 2006, pp. 649–654.